Breathing Laser-Spectral Mapping of Cavity-Enhanced Redox Reactions with Subcellular Resolution

Hui Zhu,[#] Guocheng Fang,[#] Ningyuan Nie, Jun Xie, Po-Hao Tseng, Zhongshu Xiong, Dechen Jiang, Chang-Jie Mao, Jun-Jie Zhu, Sing Yian Chew, and Yu-Cheng Chen*

Read Online

ACCESS | Metrics & More | Article Recommendations | Supporting Information

ABSTRACT: Precise and dynamic observation of redox reactions in living organisms holds significant importance for the study of physiological processes and pathological mechanisms. However, the current technologies still make it challenging to monitor this process in a nondestructive and highly sensitive manner. Herein, we introduced a bioactive laser approach for ultrasensitive and real-time monitoring of intracellular redox reactions. Resazurin, as a popular cell viability assay reagent, has lasing behaviors and photostability, which makes it suitable for the development of bioactive lasers. Due to the strong interactions of light and matter within the laser cavity, subtle changes in resazurin concentration during the redox reaction can be translated into detectable wavelength shifts in the lasing spectrum. With narrow laser peaks, the sensing resolution can reach down to 30 pM per 10 pm wavelength shift. Combined with a scanning platform, we mapped the intracellular and intercellular heterogeneities in metabolism. Further applications in cell identification, oxidative stress assessment, and drug evaluation revealed the universal applicability of this method in cell assays and biomedical analysis, providing insights into disease diagnosis and drug screening.

KEYWORDS: microlaser, cavity, redox reaction, subcellular resolution, spectral imaging
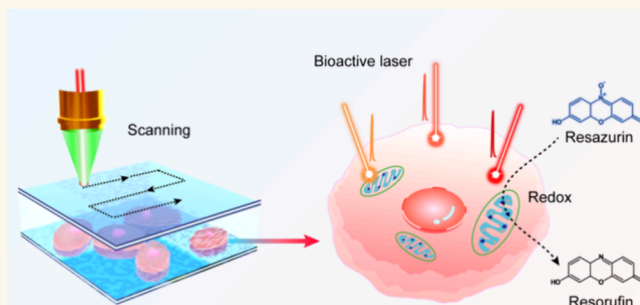
INTRODUCTION

Metabolism is the set of chemical reactions that take place within living organisms, playing a crucial role in maintaining their health and functionality.[1,2] Redox stress, even subtle change in its state, can trigger numerous physiological and pathological processes, including aging, neurodegenerative diseases, cancer, and metabolic syndrome.[3,4] Consequently, exploring and understanding the detailed redox processes associated with diseases have garnered significant attention.

Recently, a multitude of techniques, such as electrochemical methods,[5] nuclear magnetic resonance,[6,7] mass spectrometry,[8] electron paramagnetic resonance spectroscopy,[9] and colorimetry,[10] have been employed to elucidate the redox process at a small volume. However, these techniques have issues, such as causing irreversible cell damage when extracting reactant solutions within cells or masking heterogeneity in individual living cells due to sample assembly. Fluorescence characterization has become a common technique for visualizing the intracellular redox processes (e.g., reactive oxygen species (ROS), β-nicotinamide adenine dinucleotide, reduced disodium salt (NADH), and L-glutathione reduced (GSH)) within

living cells.[11,12] However, fluorescence background and the insensitive fluorescence behaviors to a tiny change may hinder some significant but inconspicuous processes,[13−16] limiting the analyzing precision at single-cell and subcellular levels.

The recent advances in optical microresonators integrated with biological materials (e.g., biomolecules, cells, tissues, and organisms) have attracted widespread interest in the fields of sensing and medicine.[17−20] The strong light−matter interactions within the optical cavity enable the amplification of subtle changes in the biological gain media,[21−23] resulting in ultrahigh sensitivity.[24−26] In particular, active resonators such as microlasers offer narrow line widths and high signal-to-noise ratios.[27,28] Currently, microlasers based on Fabry−Pérot (F−P) cavity or whispering-gallery-mode[29−33] have been success-
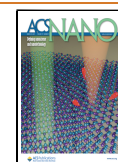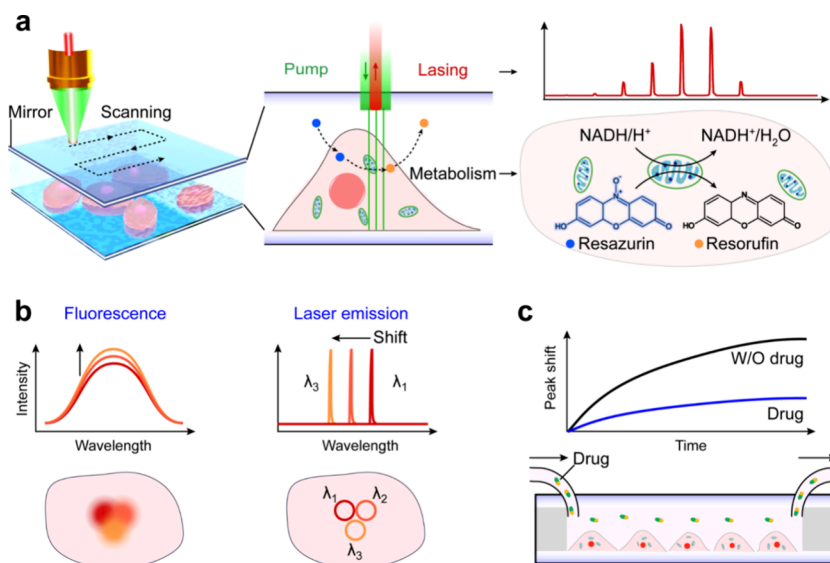
Figure 1. Concept of the bioactive laser for mapping redox reactions within the intracellular. (a) Left: experimental setup of Fabry–Pérot (F–P) cavity microlasers integrated with a scanning platform. Cells were sandwiched in two mirrors, forming the F–P cavity. Middle: real-time monitoring of cellular metabolic processes (indicated by dashed arrows) through lasing. Right: the top shows the lasing spectrum of resazurin, which served as the gain medium. The next section illustrates the detailed process of resazurin reduction through mitochondria within cells, leading to changes in the gain medium. (b) Comparison of changes between fluorescence spectrum and lasing spectrum during the metabolism. Left: slight changes in fluorescence intensity in adjacent areas make it difficult to distinguish signals in nearby regions, thereby affecting the accuracy of analysis. Right: the wavelength shift of laser emission induced by metabolism offers a more precise assessment. With the high sensitivity of laser emission technology, we can discern heterogeneity within a single cell. (c) Drug evaluation based on the bioactive laser technology.
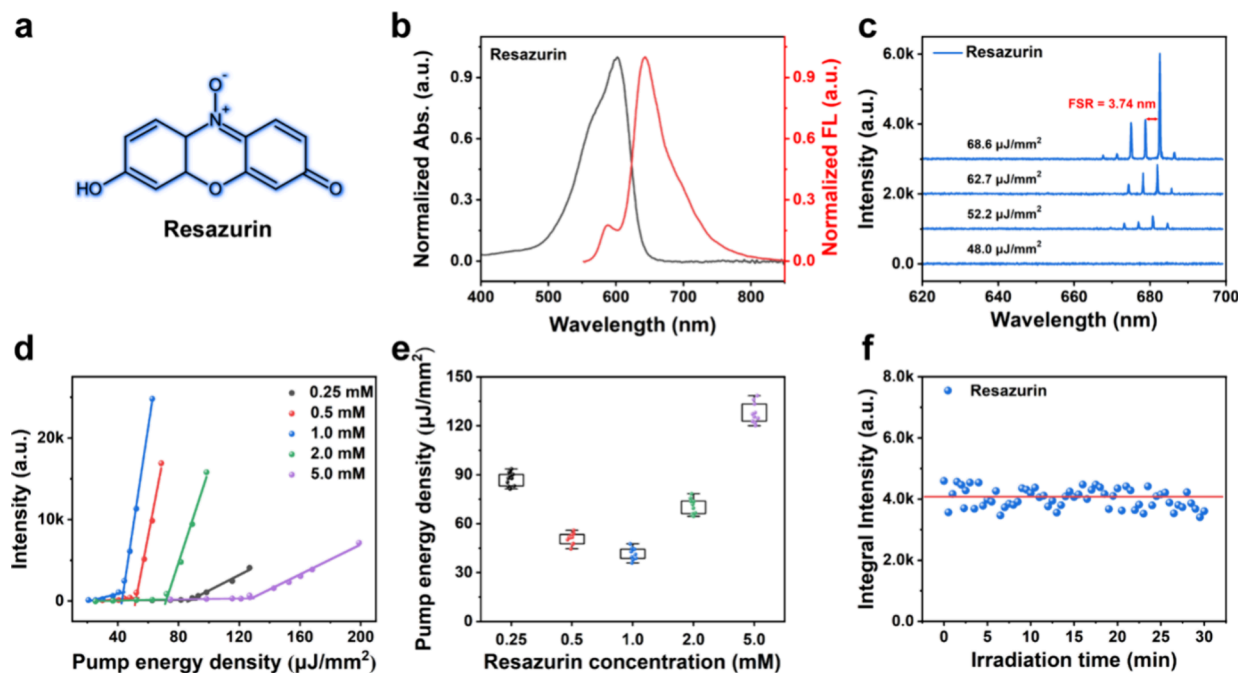

Figure 2. Bioactive laser characterization with resazurin as the gain medium. (a) Chemical structure of resazurin. (b) Normalized absorption spectrum and fluorescence spectrum of resazurin. (c) Laser emission of resazurin at different pump energy densities. (d) Lasing intensity as a function of pump energy density for various concentrations of resazurin. (e) Statistical analysis of the lasing threshold under various resazurin concentrations. (f) Stability characterization within 90,000 pulsed excitations at 1.5 times threshold pump energy density.

fully applied to various biological studies, including observing biomolecular structures,[24] detecting proteins and disease biomarkers,[21] intercellular detection,[34] cell tracking,[35,36] studying cell morphology,[25] and investigating cell contraction.[19]

In this study, we developed a bioactive laser for mapping intracellular redox activities by employing resazurin assay in an optical microresonator.[37] Redox reactions could be amplified and converted to lasing emissions for improved monitoring of chemical processes. Through the reduction of resazurin to resorufin via cellular metabolism (e.g., NADH oxidation) (Figure 1a), here, we demonstrate resazurin possesses lasing properties (Figure 1a, right) with good photostability (93%,
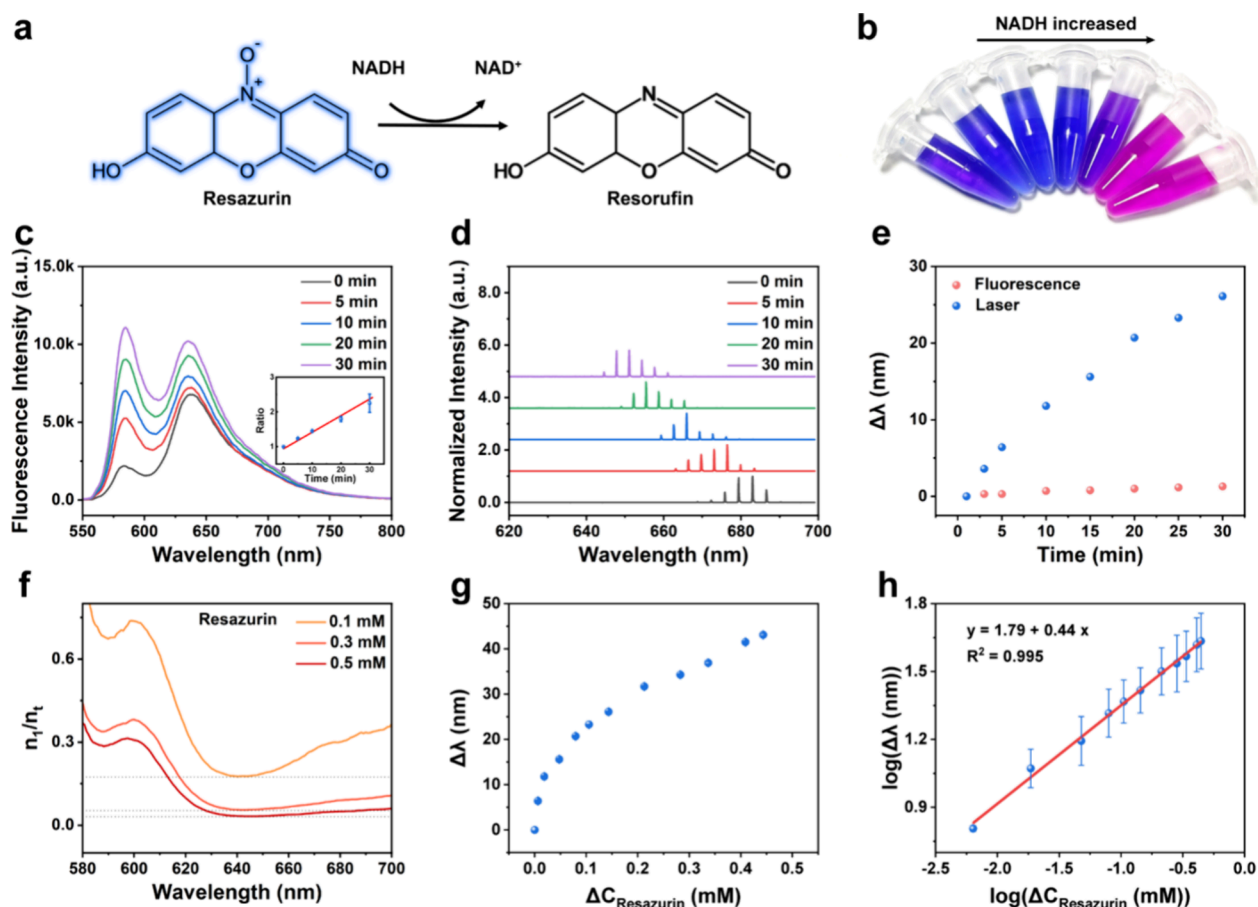
Figure 3. Bioactive laser for real-time monitoring of extracellular chemical reaction. (a) Schematic illustration of the reduction of resazurin by NADH to produce resorufin. (b) Color change was observed during the reduction of resazurin (0.5 mM) under varying NADH concentrations (0−15 mM) after 120 min. (c) Fluorescence spectra within 30 min reaction; the inset is the ratio of the enhancement of fluorescence intensity. (d) Normalized laser spectra over 30 min. (e) Wavelength shifts of fluorescence and laser spectra over 30 min. (f) Calculated population inversion required for lasing at different resazurin concentrations. (g) Experimental relationship between resazurin concentration change and laser wavelength shifts during the reaction, $N = 3$. (h) Correlation between lasing wavelength shift and changes in resazurin concentration, $N = 3$.

90000 pulses), and the lasing wavelength blue-shifted by more than 40 nm during the reduction reaction. Compared with the conventional fluorescence method (Figure 1b), the bioactive laser displayed higher sensitivity to the subtle changes in the redox reaction process due to the signal amplification effect of the F−P cavity. Capitalizing on the narrow emission and sensitive response characteristics of laser emission (Figure 1b, bottom right), combined with a scanning platform (Figure 1a, left), we effectively avoided spectral overlap and revealed the heterogeneity of reduction reactions within a single cell (Figure 1b, bottom) and between different cells (Figure 1a, left). Furthermore, this strategy has been successfully extended to oxidative stress assessment and drug valuation (Figure 1c). The bioactive laser not only is valuable for understanding cellular redox processes with subtle variations and heterogeneity but also holds great potential in biomedical applications.

RESULTS AND DISCUSSION

Lasing Behavior of Resazurin in F−P Cavity. In our study, we utilized the well-known resazurin-based cell viability assay, where resazurin exhibits an absorption peak at 601 nm (Figure 2b, Figure S1) and a fluorescence peak at 643 nm (Figure 2a and Figure S1). Typically, this assay is detected

either by observing a color change from blue to pink (Figure S1) or by measuring the fluorescence intensity of the product, resorufin (Figure S1),[37,38] which has a high quantum yield of 78%, compared to 11% for the reactant, resazurin.[39] This disparity in quantum yields limits the precision of the redox reaction analysis when using traditional methods. Nevertheless, microlasers offer the possibility to obtain more detailed redox information.

To investigate the lasing behavior of the resazurin assay, we selected the appropriately distributed Bragg reflector (DBR) (Figure S2), comprising two mirrors with high reflectivity at 590−710 and 570−700 nm, respectively. The 45 μm spacers were sandwiched between the mirrors to create the cavity used for subsequent experiments. At the optimal pump wavelength of 545 nm (Figure S2), we observed laser emission around 680 nm from the resazurin solution (Figure 2c). We further studied the lasing behavior of resazurin under various pump energy densities. Initially, no laser emission was detected, but as the pump energy density increased, the lasing intensity rose correspondingly, while the central wavelength remained stable. The free spectral range (FSR) of the lasing spectrum was measured at 3.77 nm, which closely aligned with the theoretical prediction of 3.74 nm. Additionally, we observed laser

emission from the product resorufin as well (details in Figure S2).

The lasing properties of resazurin were further examined to assess its suitability for bioanalysis. To minimize any potential impact of resazurin on cell viability (e.g., concentration and laser pump energy), we optimized the concentration. Figure 2d plots the integrated intensity of lasing as a function of pump energy density for different concentrations of resazurin. Within the range of 0.50 to 5.00 mM, the threshold pump energy reached its lowest value (43 μJ mm^{-2}) at a concentration of 1.00 mM (Figure 2e). Beyond this concentration, the threshold pump energy increased as the unexcited resazurin began to significantly contribute to cavity loss.[17] Notably, the low threshold pump energy of 52 μJ mm^{-2} at a concentration of 0.5 mM minimizes disturbance in living cell analysis, making it well-suited for the continuous and real-time monitoring of cellular processes.

In addition, photostability experiments were conducted using pulsed nanosecond laser irradiation at a repetition rate of 50 Hz and a pulse duration of 5 ns (Figure 2f and Figure S4). After 90,000 pulsed pumps with 1.5 times higher than the threshold of pump energy, the lasing intensity of resazurin remained at approximately 93%. This exceptional photostability allows for the precise identification of subtle cellular changes without introducing confounding factors, which is critical for dynamic cellular process studies and time-resolved research.

Lasing Behaviors of Redox Reaction in F−P Cavity. We first investigated the reduction reaction properties of resazurin with respect to resorufin. NADH, an important molecule crucial for metabolism with strong antioxidant abilities, serves as a reductant model (Figure 3a, Figure S6). Adding NADH to the resazurin solution changed its color from blue to pink as the NADH concentration varied (Figure 3b, Figure S5). Additionally, the 601 nm absorption peak of resazurin significantly decreased, while the 571 nm peak increased (Figure S5), suggesting that resazurin was successfully reduced to resorufin. In principle, subtle variations might result in weak changes in the fluorescence intensity and wavelength (Figure 1b). On the contrary, owing to the signal amplification effect and the narrow wavelength of laser emission, small changes could be significantly magnified (Figure 1b), displaying higher sensitivity than the fluorescence spectrum. To validate the proposed theory, we conducted both fluorescence and lasing experiments. Notably, fluorescence intensity enhancement (FL Ratio) exhibited a strong positive correlation with reaction time (Figure 3c and Figure S7a), with a fitting equation: FL ratio = 0.0477T + 0.937 (R^2 = 0.998). During the first 30 min, the fluorescence intensity increased by only 2.3-fold, accompanied by a minor wavelength shift of 1.3 nm (Figure 3c,e and Figure S7). These results indicate that neither intensity nor wavelength shifts in fluorescence provide sufficient sensitivity to detect subtle changes. In contrast, the lasing spectrum exhibited a significant wavelength shift (Figure 3d,e and Figure S7). Within the initial 30 min of the reaction, a pronounced blue shift of 26.1 nm was observed (Figure 3e), demonstrating over 10-fold greater sensitivity compared to fluorescence within the same period. This highlights the superior potential of laser emission spectra for high-sensitivity sensing applications.

To comprehensively elucidate the underlying mechanisms behind the lasing wavelength shift, we employed theoretical models to explain this phenomenon.[21] The laser rate equation model is used to delineate the relationship between the laser threshold (laser wavelength) and concentration. As depicted in the following equation at the laser threshold:

$$n_1\sigma_e(\lambda_L) = (n_t - n_1)\sigma_a(\lambda_L) + \frac{2\pi n}{\eta Q_o} \qquad (1)$$

where n_t represents the total concentration of resazurin and n_1 represents the concentration of resazurin in the excited state. $\sigma_a(\lambda_L)$ and $\sigma_e(\lambda_L)$ are the resazurin absorption and emission cross sections at the lasing wavelength (λ_L). η is the fraction of the light ($\sim$10%) and Q_0 is the average Q-factor in F−P cavity ($\sim$5 × 10^4). n is the refractive index of the resazurin ($n \approx 1.33$ for aqueous solution). By rewriting eq 1, the fractional of resazurin at the excited state can be described, γ_{th}:

$$\gamma\text{th} = \frac{n_1}{n_t} = \frac{1}{\sigma_e(\lambda) + \sigma_a(\lambda)}\left[\sigma_a(\lambda) + \frac{2\pi n}{n_1\lambda\eta Q_0}\right] \qquad (2)$$

The γ_{th} values for various concentrations of resazurin are plotted in Figure 3f based on eq 2. It is crucial to highlight that the minimum value of γ_{th} corresponds to the necessary population inversion at the lasing threshold; it also corresponds to the dominant oscillation wavelength (predicted lasing wavelength). We conducted the experiments in situ, thus, all parameters remained constant except for the concentration of resazurin during the reaction process. This allows the stable sensitive response to any changes in the resazurin concentration. At a relatively high resazurin concentration (0.5 mM) (Figure 3f, Figure S8), the γ_{th} from 635 to 690 nm remains almost constant, implying that laser emission may occur around 690 nm. As the concentration is reduced to 0.3 mM, the γ_{th} of the 635 nm band becomes slightly lower than that of the 690 nm band. The concentration of resazurin is further decreased to 0.1 mM, the γ_{th} of the 635 nm band is significantly lower than that of the 690 nm band. This observation indicates that the laser emission first appears around 635 nm at lower resazurin concentrations. In other words, as the concentration of resazurin decreases, the laser emission undergoes a blue shift from 690 to 635 nm when the pump power exceeds the threshold. Theoretically, within a certain concentration range, increasing dye concentration reduces the distance between dye molecules. This strengthens intermolecular interactions like hydrogen bonding and van der Waals forces, altering molecular electron cloud distribution and energy level structure. As a result, the energy gap between the excited state and the ground state narrows. According to the photon energy formula E = hc/λ, this indicates that the energy of the emitted photons decreases, causing the laser emission wavelength to shift toward the longer-wavelength direction, showing a positive correlation between gain medium concentration change and wavelength shift.[17,24] In this study, both theoretical simulations (Figure 3f and Figure S8) and experimental results (Figure 3d) consistently demonstrate that when decreasing the concentration of resazurin, the laser emission wavelength exhibits a blue shift. This finding validated the relationship between dye concentration and emission wavelength, emphasizing the impact of concentration on lasing wavelength, which is favorable for real-time study of redox reactions.

Leveraging the lasing wavelength shift of the reactant resazurin, spanning over 40 nm during the whole reaction as a sensing signal, holds great potential for quantifying changes in substance concentration during the reaction (Figures S7 and
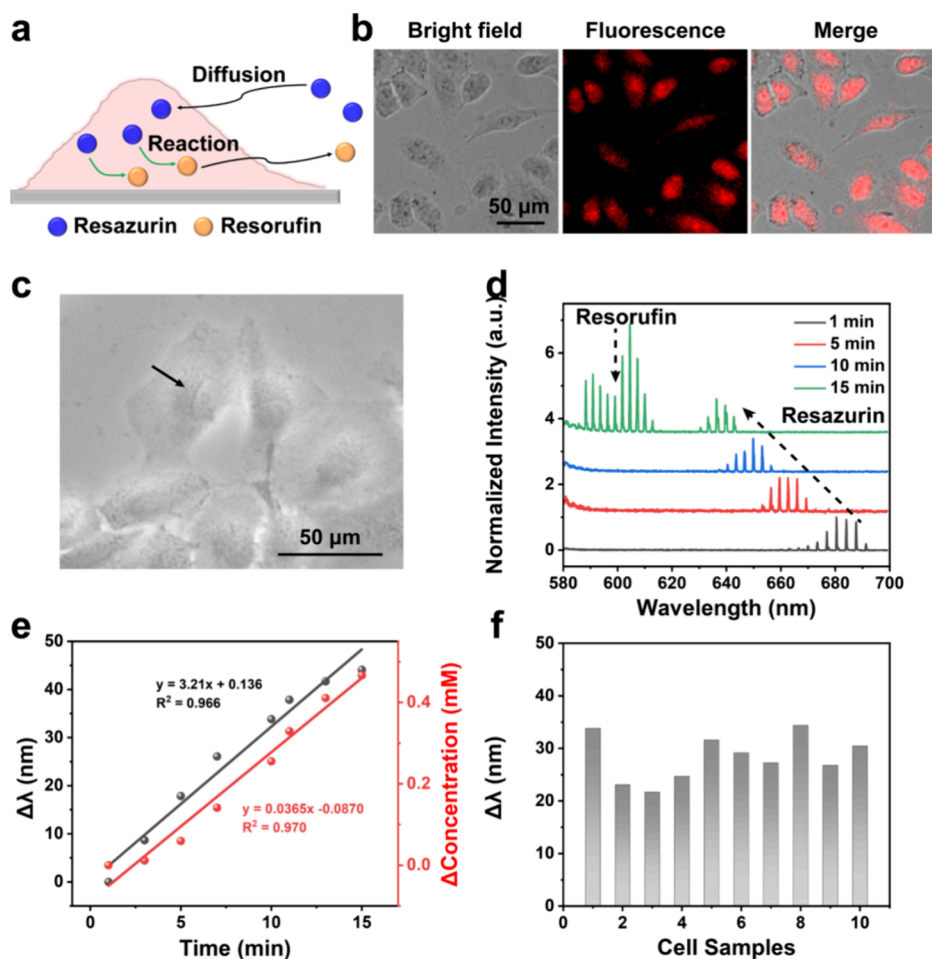
Figure 4. Bioactive laser for real-time monitoring of the intracellular redox reaction. (a) Schematic pathways of intracellular resazurin reduction. (b) Bright-field and fluorescence images of cells after adding 0.5 mM resazurin. (c) Bright-field image of A549 cells. With the laser irradiation position indicated by the black arrow. (d) Normalized lasing emission spectra of the cell reduction reaction over 15 min. (e) Wavelength shift ($\Delta\lambda$) curve (black line) and corresponding concentration change (ΔC) curve (red line) during the reaction. (f) Statistics of lasing wavelength shifts from different cell samples after 10 min of the reaction.

S9, red dot). To quantify changes in resazurin concentration, first, the absorption spectrum was used to quantitatively calibrate the resazurin concentration, as illustrated in Figure S9. The characteristic absorption peak at 601 nm served as the calibration, displaying an excellent linear relationship within the concentration range of 0.05–1.0 mM (Figure S9). Subsequently, the absorption spectrum was applied to monitor the chemical reaction between resazurin and NADH (Figure S9). In the initial 10 min, subtle changes were observed in the absorption peak, after which the peak intensity gradually decreased until 120 min. Therefore, a correlation curve of resazurin concentration versus time was generated (Figure S9, blue dot). Furthermore, based on the lasing wavelength shift and time change curve under identical conditions (Figures S7 and S9, red dot), we ultimately derived the relationship curve between wavelength shift and resazurin concentration change (Figure 3g and Figure S9). Taking a logarithm of the wavelength change ($\Delta\lambda$) and concentration change (ΔC) in Figure 3g, a linear correlation curve was achieved with eq 3 (Figure 3h, Figure S9):

$$\log(\Delta\lambda) = 1.79 + 0.44\log(\Delta C_{\text{resazurin}})$$

$$(0.05 \text{ mM} - 0.50 \text{ mM}, R^2 = 0.995, N = 3) \qquad (3)$$

As shown in Figure 3g, the lasing wavelength exhibited a substantial shift of 6.4 nm in response to a minor change in resazurin concentration from 0.50 to 0.4936 mM ($\Delta C = 0.0064$ mM). The limit of detection (LOD), defined as S/N = 3, was calculated to be 30 pM, based on the wavelength resolution of 10 pm. This result highlights the exceptional sensitivity of the lasing spectrum as a sensing signal.

Additionally, using a data processing approach similar to that applied to laser emission wavelength shifts, we successfully achieved a dual Y-axis curve illustrating the fluorescence intensity enhancement ratio (FL ratio) and the change in resazurin concentration (ΔC) over time (Figure S9g). Consequently, the relationship between the FL ratio and ΔC was established (Figure S9h). By applying a logarithmic transformation to both the FL ratio and ΔC in Figure S9h, an exponential correlation curve was obtained, expressed as log (FL ratio) = $0.107 + 1.467e^{(\log (\Delta C))/0.456}$ ($R^2 = 0.983$) (Figure S9i). When the resazurin concentration decreased from 0.5 to 0.4936 mM, the fluorescence intensity increased by only 1.23-fold, indicating relatively low sensitivity to minor changes in resazurin concentration.

Lasing Behaviors of Redox Processes in a Single Cell. The reduction performance of resazurin in vivo was investigated, as shown in Figure 4. Resazurin serves as a cell-
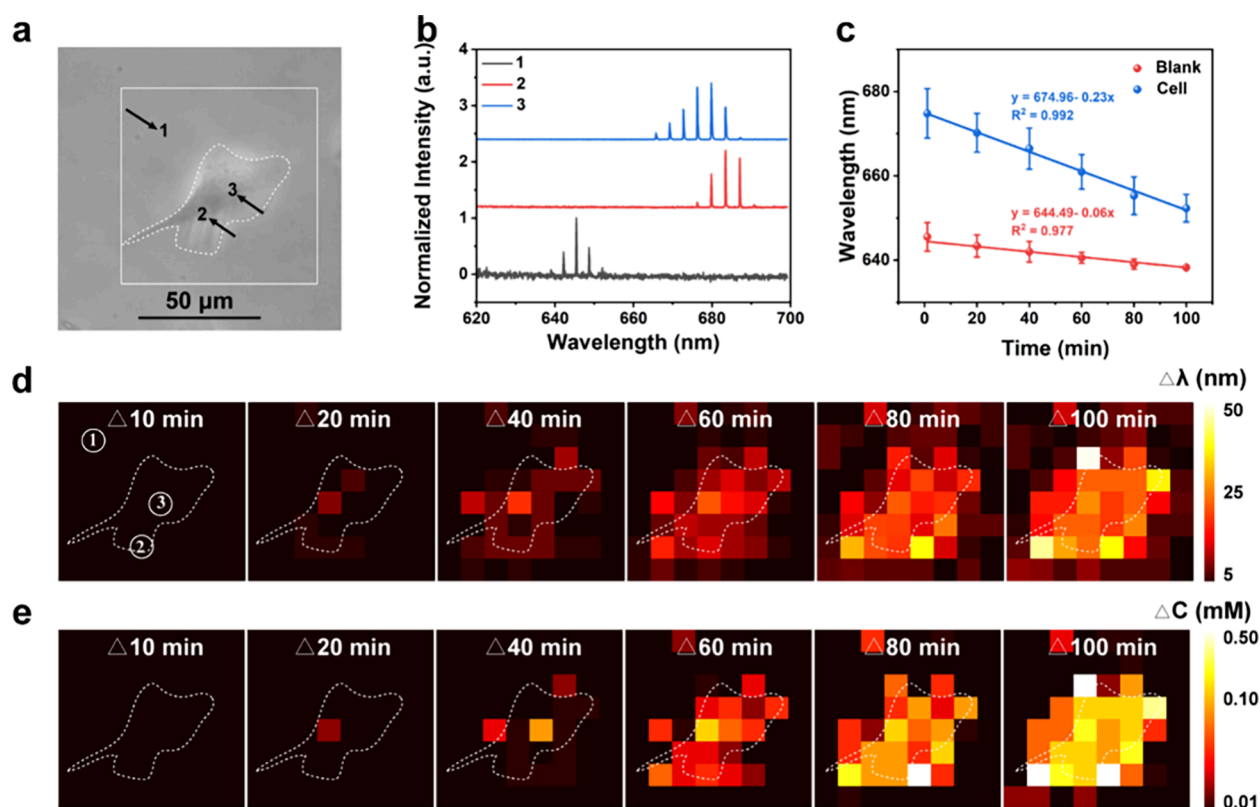
Figure 5. Spatial mapping of redox reaction by lasing wavelength shifts in A549 cells. (a) Bright-field image of a cell. The white frame indicates the scanning area with a spatial resolution of 10 μm. (b) Laser spectra corresponding to the marked positions 1, 2, and 3 in panel (a). (c) Time-dependent curve showing the lasing wavelengths for both intracellular and extracellular regions. (d) Selected frames from the $\Delta\lambda$ heatmaps of an A549 cell, showing the wavelength difference caused by the heterogeneity of chemical reactions. (e) Heatmaps displaying concentration changes with the cell, calculated using eq 3.

permeable dye that can pass through the membrane and enter the cells after being added into the cell culture medium[40] and then undergoes reduction reaction by intracellular antioxidant agents, including NADH, GSH, cysteine, and others, leading to the generation of resorufin (Figure 4a, Figure S10). The cell permeability property is similar to the free diffusion, and the diffusion distance (Δ) of resazurin within a given time (t) can be calculated according to the diffusion equation:[41,42]

$$\Delta = (2Dt)^{0.5} \qquad (4)$$

D is the diffusion coefficient for resazurin (8.5×10^{-7} cm^2 s^{-1}).[42] Within 1 min, the diffusion distance of resazurin is 102 μm, which is much larger than the size of the cell and can fully diffuse within the cell, eliminating the inaccuracies in fluorescence intensity and lasing wavelength caused by uneven diffusion. Confocal fluorescence experiments (Figure 4b, Figure S10) confirmed the in vivo reduction reaction. As the reaction proceeded, fluorescence from cells was observed approximately 6 min into the reaction (Figure S10). However, strong background fluorescence could not be ignored, resulting in a very low signal-to-background ratio (1.1−2.0), making it difficult to accurately monitor the redox process and obscuring much subtle biological information. We further statistically analyzed the fluorescence intensity from 10 different cells (Figure S10e) and plotted the fluorescence intensity as a function of time. After normalizing the initial fluorescence intensity, we obtained the curve of the FL Ratio over time (Figure S10f). By correlating this with the relationship curve between the FL ratio and ΔC (Figure S9i), we successfully

derived the relationship between ΔC and time: $\Delta C = 0.0418T - 0.0248$, $R^2 = 0.964$ (Figure S10g). This result is in high agreement with the concentration change relationship obtained from the laser emission wavelength shift ($\Delta C = 0.0365T - 0.0870$, $R^2 = 0.970$). The similar relationship curves obtained from two independent methods further confirm the correctness and reliability of using the laser emission wavelength shift to characterize changes in reactant concentration.

The bioactive lasing behavior of the intracellular reduction reaction was investigated in the F−P cavity. The effects of extracellular solutions (such as phosphate-buffered saline solution, cell culture medium, and cultured cell solution) on laser response were excluded (Figure S11). For cell experiments, A549 cells were chosen as a model and cultured on a DBR mirror. Subsequently, the resazurin solution was injected into the F−P cavity. The individual cell was illuminated (Figure 4c, black arrow), and continuous acquisition of the lasing spectrum was undertaken for dynamic investigations (Figure S12). After normalizing the laser spectral, a distinct blue shift from 680 to 640 nm was observed during the reaction (Figure 4d). At 15 min, a laser emission at 590 nm was contemporaneously detected, associated with the intracellular reduction of resazurin to resorufin. We introduced other dyes (e.g., fluorescein isothiocyanate, rhodamine 6G, and rhodamine B) as gain media to confirm that the substantial wavelength shift was attributed to the cellular reduction reaction rather than cellular activities (Figure S13). Figure 4e provides the details of the wavelength shift during the reaction. A linear relationship ($\Delta\lambda = 0.136 + 3.21x$ ($R^2 = 0.966$) was
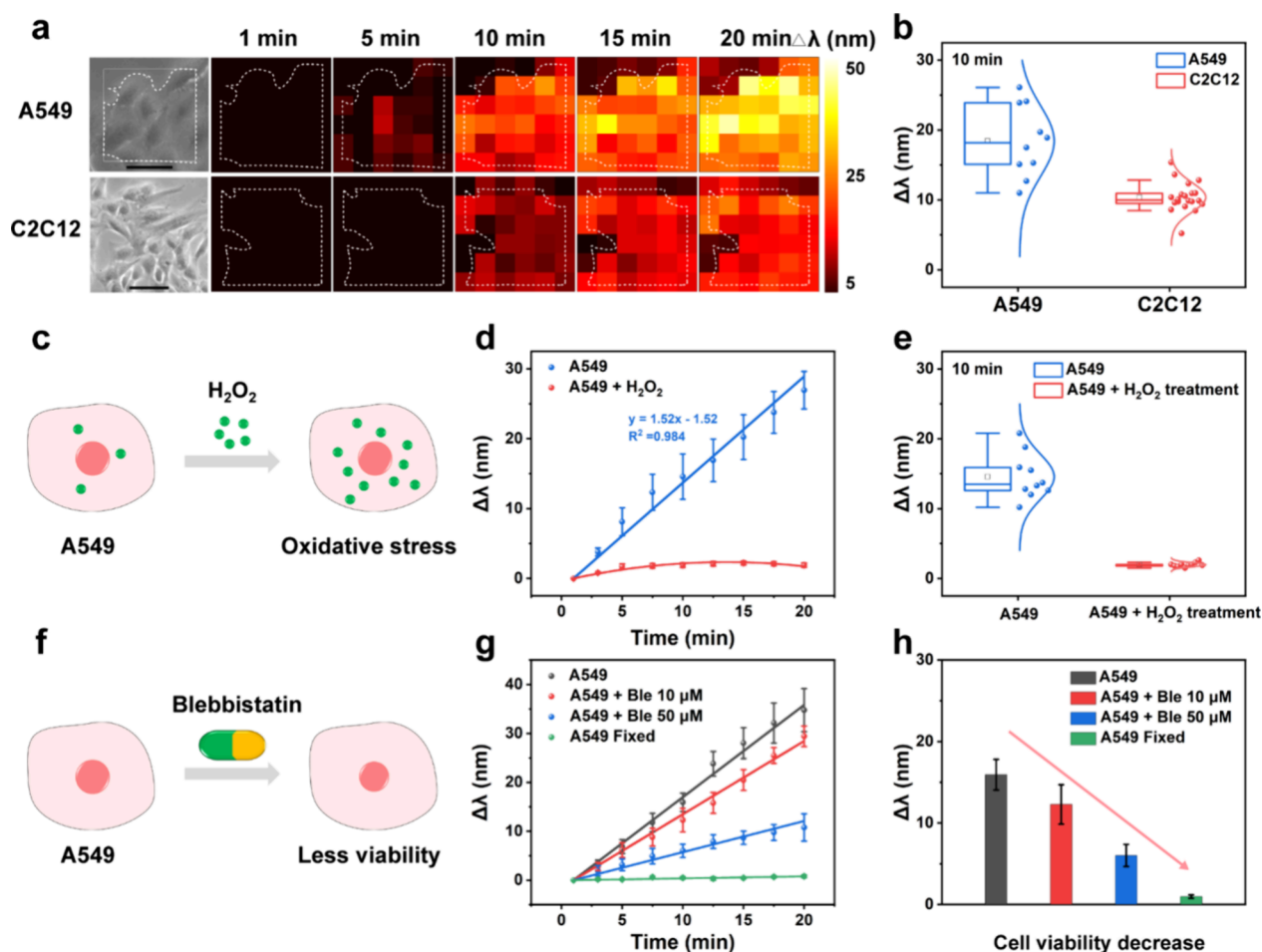
Figure 6. Evaluation of cellular stress and drug efficiency. (a) Spatial heatmap for A549 and C2C12 cells. (b) Statistic analysis of the $\Delta\lambda$ in A549 and C2C12 cells during a 10 min reaction. (c) Illustration showing the treatment of A549 cells with H_2O_2 to enhance the oxidative capacity. (d) $\Delta\lambda$ of cells over 20 min, comparing those treated with H_2O_2 and untreated cells. (e) Statistic analysis of the $\Delta\lambda$ in A549 cells with and without H_2O_2 treatment during a 10 min reaction. (f) Illustration showing the treatment of A549 cells with different concentrations of the drug. (g) $\Delta\lambda$ of the cells over 20 min with different drug concentrations. The fixed cells were utilized as the control group. (h) Statistic analysis of $\Delta\lambda$ corresponding to varying drug concentrations during a 10 min reaction.

obtained (Figure 4e, black curve). Then, the change in resazurin concentration (ΔC) within cells (Figure 4e, red curve) was derived by using eq 3. Similarly, a positive linear correlation ($\Delta C = -0.0870 + 0.0365x$, $R^2 = 0.970$) existed between the ΔC and time. An 11.5 μM change in resazurin concentration led to a nearly 9 nm wavelength shift, again supporting the highly sensitive response of wavelength shifts to subtle concentration changes. The shift in lasing wavelength was observed across a broader sample of A549 cells. $\Delta\lambda$ was statistically analyzed after 10 min of reaction (Figure 4f). These wavelength shifts exhibited apparent heterogeneity, suggesting the diverse reducing abilities present across cells.

To fully illustrate the versatility of the bioactive laser approach for monitoring cellular redox reactions, different cell types and oxidative stress dyes were selected. Mouse myoblast cell line C2C12 was chosen. After 0.5 mM resazurin was introduced, a noticeable lasing wavelength shift was observed (Figure S14), indicating universality. Intriguingly, the wavelength shift of C2C12 cells was markedly distinct from A549 cells. Details are given in Figure 6a. In addition to the aforementioned changes in lasing behavior resulting from reduction reactions, oxidation reactions within cells may also induce alterations in lasing behavior. Dichlorofluorescin

(DCFH), an oxidative stress dye was selected.[43] When mixed with A549 cells, DCFH undergoes oxidation to produce a robust fluorescent substance, 2′-7′dichlorofluorescein (DCF),[43] which emits lasing (Figure S15), demonstrating the feasibility of oxidation reactions in biological research. Bioactive lasers exhibit the capability to monitor intracellular redox reactions, revealing their significant potential in advancing the study of cellular biochemical reactions.

Spatial Mapping of Redox Reaction within a Single Cell. To enhance the comprehension of the heterogeneity of cellular reduction, a scanning platform integrated with a laser system was applied (Figure 1a). Attributing to the narrow emission characteristics of lasers, which are only about 1 nm, bioactive laser mapping achieves higher spatial resolution than traditional fluorescence imaging. This enables the expression of heterogeneity in adjacent regions (Figure 1b). The pump beam scanning area was determined based on the size of the cell. Generally, an area of 80 μm × 80 μm is enough to scan the entire single cell (Figure S16). As the excitation beam scanned across the area (white frame) of the A549 cell (Figure 5a), lasing wavelength with fixed spatial resolution can be generated and acquired immediately. The lasing wavelength was varied from different regions (Figure 5b and Figure S16), which may

be attributed to the heterogeneity of intracellular activities (e.g., energy requirements, cell state, intracellular environment, etc.).[44] Within the 100 min reaction time, the lasing wavelength on the cells blue-shifted from 675 to 652 nm (difference: 23 nm), and the lasing wavelength in the solution blue-shifted from 645 to 638 nm (difference: 7 nm) (Figure 5c). The lasing wavelength change in the cells is more than three times that in the solution, displaying a high signal-to-background ratio. This phenomenon can be explained by the theoretical simulations in Figure 3f and Figure S8. Upon introducing resazurin into the cellular environment, the cells serve as reactors, and more resazurin accumulates inside the cell; consequently, concentration changes larger within them. The concentration changes of resazurin correlated positively with the wavelength shift (Figures 3h and 4e). As a result, the laser wavelength changes observed in cells are more pronounced compared with those in the solution, providing the possibility of single-cell mapping.

Figure 5d depicts the $\Delta\lambda$ mapping of a single cell. To acquire as many images of a single cell as possible, we reduced the number of cells on the DBR to slow the reaction rate. The original data heatmap images are presented in Figure S16. As the reduction reaction advanced, the lasing wavelength gradually blue-shifted. By subtracting the wavelength recorded in the first minute from the spectral wavelengths obtained at different times, we gained $\Delta\lambda$ imaging corresponding to different times (Figure 5d). Significantly, $\Delta\lambda$ varied greatly in different regions, showing the heterogeneity of reaction rates. Increasing the spatial resolution from 20 to 2.5 μm, the heterogeneity of wavelength shifts was observed from spectral images (Figures S16−S19). In addition, $\Delta\lambda$ heatmaps were converted into ΔC heatmaps (Figure 5e) using eq 3, revealing that small concentration changes correspond to significant wavelength changes and highlighting the high sensitivity of the lasing method. Furthermore, concentration changes varied in different regions of the cell, confirming the heterogeneity in reaction rates. Collectively, these results elucidated the advantages of bioactive lasers for monitoring redox reactions, showcasing high sensitivity and spatial resolution.

Evaluation of Cellular Stress and Drug Efficiency. We further applied this technique in a cell assay for cellular stress and drug evaluation. For example, based on earlier experiments (Figures S12 and S14), it was observed that A549 cells induced more substantial changes in lasing wavelength compared to C2C12 cells over the same time duration. A spatial mapping platform was employed to validate and confirm this result (Figure 6a, Figures S20 and S21). Compared to C2C12 cells ($\Delta\lambda$ = 10 nm, 10 min), tumor cells A549 showed a more substantial change in laser wavelength ($\Delta\lambda$ = 19 nm, 10 min) (Figure 6a,b) within the same reaction time. This was attributed to the strongly reducing environment within A549 cells, primarily resulting from the overproduction of intracellular GSH.[45] The sensitive response to the internal environment enabled effective cell recognition. Moreover, A549 cells also exhibit overproduction of ROS, resulting in increased oxidative stress.[45] To verify this, hydrogen peroxide (H_2O_2, 10 mM, 5 min) stimulation was employed to elevate intracellular H_2O_2 levels in A549 cells (Figure 6c). After that, the stimulated cells exhibited only a mild lasing wavelength shift (2 nm) (Figure 6d,e), confirming the oxidative stress response of A549 cells. In addition, this method can also be used for drug efficacy evaluation (Figure 6f,h, Figure S22).[46] Taking blebbistatin (Ble) as a model, which is a commonly

used protease activity inhibitor,[47,48] we regulate cell activity by adjusting the concentration of Ble (10 and 50 μM, respectively). Cells treated with higher Ble concentrations displayed smaller wavelength shifts. The experiments in drug evaluation further showed the acceptable repeatability of the bioactive lasers (Figure S23), proving the drug effect on cell viability and suggesting the potential of this bioactive laser approach to evaluate drug efficacy. These applications evidence that the bioactive laser method has great potential in biological investigation via redox analysis.

CONCLUSIONS

In summary, we devised a bioactive laser platform that can be used to monitor redox reactions within cells. The laser emission behavior was investigated under redox reactions, revealing good stability with 93% emission retention after 90,000 pulses of laser irradiations. During redox reactions, the lasing spectrum exhibited ultrahigh sensitivity to small changes in resazurin concentration, achieving a resolution of 30 pM per 10 pm wavelength shift far superior to the traditional fluorescence method. By leveraging the narrow emission characteristics of laser spectroscopy, we uncovered the heterogeneity in the reduction capabilities among cell microdomains and individual cells. This bioactive laser approach proved to be effective for various applications, including cell identification, oxidative stress assessment, and drug evaluation. The highly sensitive laser response to subtle changes provides a powerful platform for exploring cellular dynamics with unprecedented detail, offering new insights into intricate cellular processes and paving the way for advances in biological research and clinical applications.

MATERIALS AND METHODS

Chemicals. Resazurin sodium salt, resorufin sodium salt, magnesium chloride ($MgCl_2$), sodium chloride (NaCl), calcium chloride ($CaCl_2$), silver chloride (AgCl), potassium chloride (KCl), potassium thiocyanate (KSCN), sodium thiosulfate ($Na_2S_2O_3$), hydrogen peroxide solution (H_2O_2), L-tryptophan (Trp), L-leucine (Leu), L-histidine (His), L-homocysteine (Hcy), L-cysteine (Cys), L-glutathione reduced (GSH), fluorescein isothiocyanate (FITC), rhodamine 6G (Rh6G), rhodamine B (RhB), dichlorofluorescin (DCFH), β-nicotinamide adenine dinucleotide, and reduced disodium salt (NADH) were purchased from Sigma-Aldrich. All of the other chemical reagents of analytical grade were used as received without further purification.

Fabry−Pérot (F−P) Cavity Fabrication. The F−P cavity setup is illustrated in Figure 1. Briefly, two highly reflective dielectric mirrors (distributed Bragg reflector, DBR) with a reflectivity of 99.9% (560−675 and 580−710 nm) were used. The chemical reaction was conducted by sandwiching the solution and cells between two DBRs, with 45 μm diameter glass beads used as spacers to fix the cavity length.

Absorption Measurement. The absorbance (A) was measured using a NanoDrop 2000c spectrophotometer (Thermal Scientific) to identify the dyes resazurin and resorufin, enabling tracking of the dynamic resazurin reduction reaction.

Cell Culture on DBR. To culture cells on the DBR, the mirrors were first sterilized with 75% ethanol. After sterilization, the DBR mirrors were immersed in the cell culture medium to prepare for cell seeding. Cells were then loaded onto the mirrors, and after 24 h of incubation, they successfully adhered and spread across the mirror surface. The culture medium used was DMEM, supplemented with 10% fetal bovine serum (FBS) and 100 U mL^{-1} penicillin/streptomycin. The cells were cultured in a standard incubator at 37 °C with 5% CO_2.

Drug Treatment. The cells were treated with 10 and 50 μM blebbistatin (Sigma-Aldrich), respectively. After 24 h of incubation, the cells on the DBR mirrors were analyzed using the laser system.

Optical System Setup. As depicted in Figure 1, an upright microscopic system (Nikon Ni2) equipped with a 20× (0.4 NA) objective lens was utilized for both the optical pumping of the molecules and the collection of emitted light. Optical pumping was achieved by a pulsed nanosecond laser (EKSPLA PS8001DR) integrated with an optical parametric oscillator, operating at a repetition rate of 50 Hz and a pulse duration of 5 ns. The pump laser wavelength was optimized for resazurin and resorufin, with the setting at 545 nm for the relevant experiments. The pump energy density was adjusted by varying the neutral density filter. At the focal plane of the objective, the beam diameter was approximately 20 μm when the excitation beam was focused at the center of the analyte. Emission photos were collected through the same objective, then separated by a beam splitter (567 nm dichroic mirror), and finally transmitted to either a charge-coupled device camera or an imaging spectrometer (Andor Kymera 328i and Newton 970 EMCCD). Fluorescence spectra were acquired through a similar setup with an LED serving as the pump source instead of a nanosecond laser. Fluorescence images were captured by a CCD camera (Andor Zyla SCMOS) mounted on the microscope.

Cell Mapping. We manually coded a small program to control the displacement stage for achieving two-dimensional spectral imaging. By adjusting the step size of the movement, we can finely tune the spatial resolution of the cell imaging. The spatial resolution can span from different areas of a single cell to different cells, enabling real-time monitoring of intra- and intercell heterogeneity. This capability provides possibilities for cell identification, drug evaluation, and other applications.

Calculation of Required Population Inversion (Threshold) (Theoretical Analysis). Based on the absorption and emission spectra of resazurin (or resorufin), the derived absorption cross section and emission cross section can be derived.[49] In particular, the absorption cross section ($\sigma_a (\lambda)$ of resazurin (or resorufin) can be calculated by

$$\sigma_a(\lambda) = 3.8 \times 10 - 21\varepsilon(\lambda)$$

where ε is the extinction coefficient and is derived from the absorbance (A). Here $A = [\text{resazurin}]\varepsilon L$, where [resazurin] is the concentration of resazurin and L is the optical path ($L = 1$ mm).

The emission cross section of a laser transition $\sigma_e (\lambda)$ can be derived from the fluorescence spectrum and the quantum yield:

$$\sigma_e(\lambda) = \frac{\lambda^4 E(\lambda)}{8\pi c n^2 \tau_F}$$

where $E(\lambda)$ is the fluorescence quantum distribution of resazurin. It is proportional to the fluorescence intensity but normalized to the quantum yield, q, i.e., $\int E(\lambda)d\lambda = q$ ($q = 0.11$ for resazurin, $q = 0.70$ for resorufin; both are in water at pH 7.4). τ_F is the fluorescence lifetime ($\tau_F \approx 0.7$ ns for resazurin, $\tau_F \approx 3.0$ ns for resorufin). c is the speed of light in vacuum, and n is the surrounding medium refractive index ($n = 1.33$ for water).

To illustrate the laser switching behavior, we performed a theoretical analysis of resazurin (and resorufin) population inversion. We carried out the laser rate equations based on resazurin (or resorufin) molecules. Under steady-state conditions, which correspond to the lasing threshold,

$$n_1\sigma_e(\lambda_L) = (n_T - n_1)\sigma_a(\lambda_L) + \frac{2\pi n}{\eta Q_o}$$

By rearranging the equation, the fractional resazurin (and resorufin) at the excited state can be expressed by,

$$\frac{n_1}{n_T} = \frac{1}{\sigma_e(\lambda) + \sigma_a(\lambda)}\left[\sigma_a(\lambda) + \frac{2\pi n}{n_1\eta Q_0}\right]$$

where n_T is the total concentration of resazurin (or resorufin) and n_1 is the concentration of resazurin in the excited state. η is the fraction of the light ($\sim$10%), and Q_0 is the average Q-factor in the F–P cavity ($\sim$5 × 10^4).

ASSOCIATED CONTENT

Ⓢ Supporting Information

The Supporting Information is available free of charge at https://pubs.acs.org/doi/10.1021/acsnano.4c16389.

> Characterization of the molecular structure, color, absorption, and fluorescence spectra of dyes; characterization of the F–P cavity mirror and the laser emission of dyes; optimization of dye concentration; stability of dyes; characterization of the dynamic reaction process between resazurin and reductant in aqueous solution; theoretical calculations; characterization of the quantitative reactions; fluorescence imaging of cells; laser emission from different type cells; laser emission of different dyes within A549 cells; laser emission behavior of oxidative stress dyes; spatial heatmaps of real-time imaging of cellular reduction at different spatial resolution; spatial heatmaps of real-time imaging of 2D cells reduction; application of the bioactive laser for drug evaluation (DOCX)

AUTHOR INFORMATION

Corresponding Author

Yu-Cheng Chen − *School of Electrical and Electronics Engineering, Nanyang Technological University, Singapore 639798, Singapore;* Ⓞ orcid.org/0000-0002-0008-5601; Email: yucchen@ntu.edu.sg

Authors

Hui Zhu − *School of Electrical and Electronics Engineering, Nanyang Technological University, Singapore 639798, Singapore; Key Laboratory of Structure and Functional Regulation of Hybrid Materials (Ministry of Education), School of Chemistry & Chemical Engineering, Anhui University, Hefei, Anhui 230601, China;* Ⓞ orcid.org/0000-0003-4400-7821

Guocheng Fang − *School of Electrical and Electronics Engineering, Nanyang Technological University, Singapore 639798, Singapore*

Ningyuan Nie − *School of Electrical and Electronics Engineering, Nanyang Technological University, Singapore 639798, Singapore*

Jun Xie − *School of Electrical and Electronics Engineering, Nanyang Technological University, Singapore 639798, Singapore*

Po-Hao Tseng − *School of Electrical and Electronics Engineering, Nanyang Technological University, Singapore 639798, Singapore*

Zhongshu Xiong − *School of Electrical and Electronics Engineering, Nanyang Technological University, Singapore 639798, Singapore*

Dechen Jiang − *State Key Laboratory of Analytical Chemistry for Life Science, School of Chemistry and Chemical Engineering, Nanjing University, Nanjing, Jiangsu 210023, China;* Ⓞ orcid.org/0000-0002-2845-3621

Chang-Jie Mao − *Key Laboratory of Structure and Functional Regulation of Hybrid Materials (Ministry of Education), School of Chemistry & Chemical Engineering, Anhui University, Hefei, Anhui 230601, China;* Ⓞ orcid.org/0000-0002-5563-4153

Jun-Jie Zhu − *State Key Laboratory of Analytical Chemistry for Life Science, School of Chemistry and Chemical Engineering, Nanjing University, Nanjing, Jiangsu 210023, China;* ● orcid.org/0000-0002-8201-1285

Sing Yian Chew − *Lee Kong Chian School of Medicine, Singapore 308232, Singapore;* ● orcid.org/0000-0002-6084-5967

Complete contact information is available at:
https://pubs.acs.org/10.1021/acsnano.4c16389

Author Contributions

#H.Z. and G.F. contributed equally.

Author Contributions

H.Z. and Y.-C.C. conceived the idea and designed the experiments; H.Z., G.F., N.N., J.X., P.T., and Z.X. conducted the experiments; G.F., S.C., and N.N. helped with the analyze of the principle; D.J., C.-J.M, J.-J.Z., S.C. provided useful advice; H.Z. and Y.-C.C. wrote the paper; Y.-C.C. supervised the whole project.

Notes

The authors declare no competing financial interest.

REFERENCES

(1) Sies, H.; Jones, D. P. Reactive oxygen species (ROS) as pleiotropic physiological signalling agents. *Nat. Rev. Mol. Cell Biol.* **2020**, *21* (7), 363−383.

(2) Covarrubias, A. J.; Perrone, R.; Grozio, A.; Verdin, E. NAD(+) metabolism and its roles in cellular processes during ageing. *Nat. Rev. Mol. Cell Biol.* **2021**, *22* (2), 119−141.

(3) Bešlo, D.; Golubić, N.; Rastija, V.; Agić, D.; Karnaš, M.; Šubarić, D.; Lučić, B. Antioxidant Activity, Metabolism, and Bioavailability of Polyphenols in the Diet of Animals. *Antioxidants* **2023**, *12* (6), 1141.

(4) Jomova, K.; Raptova, R.; Alomar, S. Y.; Alwasel, S. H.; Nepovimova, E.; Kuca, K.; Valko, M. Reactive oxygen species, toxicity, oxidative stress, and antioxidants: chronic diseases and aging. *Arch. Toxicol.* **2023**, *97* (10), 2499−2574.

(5) Malferrari, M.; Becconi, M.; Rapino, S. Electrochemical monitoring of reactive oxygen/nitrogen species and redox balance in living cells. *Anal. Bioanal. Chem.* **2019**, *411* (19), 4365−4374.

(6) Rhieu, S. Y.; Urbas, A. A.; Bearden, D. W.; Marino, J. P.; Lippa, K. A.; Reipa, V. Probing the intracellular glutathione redox potential by in-cell NMR spectroscopy. *Angew. Chem., Int. Ed. Engl.* **2014**, *53* (2), 447−450.

(7) Mochizuki, A.; Saso, A.; Zhao, Q.; Kubo, S.; Nishida, N.; Shimada, I. Balanced Regulation of Redox Status of Intracellular Thioredoxin Revealed by in-Cell NMR. *J. Am. Chem. Soc.* **2018**, *140* (10), 3784−3790.

(8) Su, Z.; Burchfield, J. G.; Yang, P.; Humphrey, S. J.; Yang, G.; Francis, D.; Yasmin, S.; Shin, S. Y.; Norris, D. M.; Kearney, A. L.; Astore, M. A.; Scavuzzo, J.; Fisher-Wellman, K. H.; Wang, Q. P.; Parker, B. L.; Neely, G. G.; Vafaee, F.; Chiu, J.; Yeo, R.; Hogg, P. J.; Fazakerley, D. J.; Nguyen, L. K.; Kuyucak, S.; James, D. E. Global redox proteome and phosphoproteome analysis reveals redox switch in Akt. *Nat. Commun.* **2019**, *10* (1), 5486.

(9) Lin, L.; Pang, W.; Jiang, X.; Ding, S.; Wei, X.; Gu, B. Light amplified oxidative stress in tumor microenvironment by carbonized hemin nanoparticles for boosting photodynamic anticancer therapy. *Light: Sci. Appl.* **2022**, *11* (1), 47.

(10) Noacco, N.; Rodenak-Kladniew, B.; de Bravo, M. G.; Castro, G. R.; Islan, G. A. Simple colorimetric method to determine the in vitro antioxidant activity of different monoterpenes. *Anal. Biochem.* **2018**, *555*, 59−66.

(11) Zou, Y.; Wang, A.; Shi, M.; Chen, X.; Liu, R.; Li, T.; Zhang, C.; Zhang, Z.; Zhu, L.; Ju, Z.; Loscalzo, J.; Yang, Y.; Zhao, Y. Analysis of redox landscapes and dynamics in living cells and in vivo using genetically encoded fluorescent sensors. *Nat. Protoc.* **2018**, *13* (10), 2362−2386.

(12) Geng, Y.; Wang, Z.; Zhou, J.; Zhu, M.; Liu, J.; James, T. D. Recent progress in the development of fluorescent probes for imaging pathological oxidative stress. *Chem. Soc. Rev.* **2023**, *52* (11), 3873−3926.

(13) Hulspas, R.; O'Gorman, M. R. G.; Wood, B. L.; Gratama, J. W.; Sutherland, D. R. Considerations for the control of background fluorescence in clinical flow cytometry. *Cytometry, Part B* **2009**, *76* (6), 355−364.

(14) Gao, P.; Prunsche, B.; Zhou, L.; Nienhaus, K.; Nienhaus, G. U. Background suppression in fluorescence nanoscopy with stimulated emission double depletion. *Nat. Photonics* **2017**, *11* (3), 163−169.

(15) Jiang, Y.; Pu, K. Molecular Probes for Autofluorescence-Free Optical Imaging. *Chem. Rev.* **2021**, *121* (21), 13086−13131.

(16) Hou, Y.; Wang, D.; Lu, S.; Guo, D.; Li, M.; Cui, M.; Zhang, X. E. Optogenetic Control of Background Fluorescence Reduction for CRISPR-Based Genome Imaging. *Anal. Chem.* **2022**, *94* (24), 8724−8731.

(17) Gather, M. C.; Yun, S. H. Single-cell biological lasers. *Nat. Photonics* **2011**, *5* (7), 406−410.

(18) Humar, M.; Yun, S. H. Intracellular microlasers. *Nat. Photonics* **2015**, *9* (9), 572−576.

(19) Schubert, M.; Woolfson, L.; Barnard, I. R. M.; Dorward, A. M.; Casement, B.; Morton, A.; Robertson, G. B.; Appleton, P. L.; Miles, G. B.; Tucker, C. S.; Pitt, S. J.; Gather, M. C. Monitoring contractility in cardiac tissue with cellular resolution using biointegrated microlasers. *Nat. Photonics* **2020**, *14* (7), 452−458.

(20) Titze, V. M.; Caixeiro, S.; Dinh, V. S.; Konig, M.; Rubsam, M.; Pathak, N.; Schumacher, A. L.; Germer, M.; Kukat, C.; Niessen, C. M.; Schubert, M.; Gather, M. C. Hyperspectral confocal imaging for high-throughput readout and analysis of bio-integrated microlasers. *Nat. Protoc.* **2024**, *19* (3), 928−959.

(21) Chen, Y. C.; Tan, X.; Sun, Q.; Chen, Q.; Wang, W.; Fan, X. Laser-emission imaging of nuclear biomarkers for high-contrast cancer screening and immunodiagnosis. *Nat. Biomed. Eng.* **2017**, *1*, 724−735.

(22) Yang, X.; Tang, S.-J.; Meng, J.-W.; Zhang, P.-J.; Chen, Y.-L.; Xiao, Y.-F. Phase-Transition Microcavity Laser. *Nano Lett.* **2023**, *23* (7), 3048−3053.

(23) Yang, X.; Gong, C.; Zhang, C.; Wang, Y.; Yan, G. F.; Wei, L.; Chen, Y. C.; Rao, Y. J.; Gong, Y. Fiber Optofluidic Microlasers: Structures, Characteristics, and Applications. *Laser Photonics Rev.* **2021**, *16* (1), No. 2100171.

(24) Gong, X.; Qiao, Z.; Liao, Y.; Zhu, S.; Shi, L.; Kim, M.; Chen, Y. C. Enzyme-Programmable Microgel Lasers for Information Encoding and Anti-Counterfeiting. *Adv. Mater.* **2022**, *34* (10), No. 2107809.

(25) Qiao, Z.; Xu, H.; Zhang, N.; Gong, X.; Gong, C.; Yang, G.; Chew, S. Y.; Huang, C.; Chen, Y. C. Cellular Features Revealed by Transverse Laser Modes in Frequency Domain. *Adv. Sci.* **2022**, *9* (1), No. 2103550.

(26) Gong, C.; Yang, X.; Tang, S.-J.; Zhang, Q.-Q.; Wang, Y.; Liu, Y.-L.; Chen, Y.-C.; Peng, G.-D.; Fan, X.; Xiao, Y.-F.; Rao, Y.-J.; Gong, Y. Submonolayer biolasers for ultrasensitive biomarker detection. *Light: Sci. Appl.* **2023**, *12* (1), 292.

(27) Fang, G.; Qiao, Z.; Huang, L.; Zhu, H.; Xie, J.; Zhou, T.; Xiong, Z.; Su, I. H.; Jin, D.; Chen, Y.-C. Single-cell laser emitting cytometry for label-free nucleolus fingerprinting. *Nat. Commun.* **2024**, *15* (1), 7332.

(28) Fang, G.; Ho, B. X.; Xu, H.; Gong, C.; Qiao, Z.; Liao, Y.; Zhu, S.; Lu, H.; Nie, N.; Zhou, T.; Kim, M.; Huang, C.; Soh, B. S.; Chen, Y.-C. Compressible Hollow Microlasers in Organoids for High-Throughput and Real-Time Mechanical Screening. *ACS Nano* **2024**, *18*, 26338−26349.

(29) He, L.; Özdemir, Ş. K.; Yang, L. Whispering gallery microcavity lasers. *Laser Photonics Rev.* **2013**, *7* (1), 60−82.

(30) Fikouras, A. H.; Schubert, M.; Karl, M.; Kumar, J. D.; Powis, S. J.; Di Falco, A.; Gather, M. C. Non-obstructive intracellular nanolasers. *Nat. Commun.* **2018**, *9* (1), 4817.

(31) Chen, Y. C.; Fan, X. Biological Lasers for Biomedical Applications. *Adv. Opt. Mater.* **2019**, *7* (17), No. 1900377.

(32) Toropov, N.; Cabello, G.; Serrano, M. P.; Gutha, R. R.; Rafti, M.; Vollmer, F. Review of biosensing with whispering-gallery mode lasers. *Light: Sci. Appl.* **2021**, *10* (1), 42.

(33) Yu, X.-C.; Tang, S.-J.; Liu, W.; Xu, Y.; Gong, Q.; Chen, Y.-L.; Xiao, Y.-F. Single-molecule optofluidic microsensor with interface whispering gallery modes. *Proc. Natl. Acad. Sci. U. S. A.* **2022**, *119* (6), No. e2108678119.

(34) Kwok, S. J. J.; Martino, N.; Dannenberg, P. H.; Yun, S. H. Multiplexed laser particles for spatially resolved single-cell analysis. *Light: Sci. Appl.* **2019**, *8*, 74.

(35) Schubert, M.; Steude, A.; Liehm, P.; Kronenberg, N. M.; Karl, M.; Campbell, E. C.; Powis, S. J.; Gather, M. C. Lasing within Live Cells Containing Intracellular Optical Microresonators for Barcode-Type Cell Tagging and Tracking. *Nano Lett.* **2015**, *15* (8), 5647−52.

(36) Tang, S. J.; Dannenberg, P. H.; Liapis, A. C.; Martino, N.; Zhuo, Y.; Xiao, Y. F.; Yun, S. H. Laser particles with omnidirectional emission for cell tracking. *Light: Sci. Appl.* **2021**, *10* (1), 23.

(37) Elavarasan, T.; Chhina, S. K.; Parameswaran, M.; Sankaran, K. Resazurin reduction based colorimetric antibiogram in microfluidic plastic chip. *Sens. Actuators, B* **2013**, *176*, 174−180.

(38) Wang, F.; Li, Y.; Li, W.; Zhang, Q.; Chen, J.; Zhou, H.; Yu, C. A facile method for detection of alkaline phosphatase activity based on the turn-on fluorescence of resorufin. *Anal. Methods* **2014**, *6* (15), 6105−6109.

(39) Bueno, C.; Villegas, M. L.; Bertolotti, S. G.; Previtali, C. M.; Neumann, M. G.; Encinas, M. V. The Excited-State Interaction of Resazurin and Resorufin with Aminesin Aqueous Solutions. Photophysics and Photochemical Reaction¶. *Photochem. Photobiol.* **2002**, *76* (4), 385−390.

(40) Lavogina, D.; Lust, H.; Tahk, M. J.; Laasfeld, T.; Vellama, H.; Nasirova, N.; Vardja, M.; Eskla, K. L.; Salumets, A.; Rinken, A.; Jaal, J. Revisiting the Resazurin-Based Sensing of Cellular Viability: Widening the Application Horizon. *Biosensors* **2022**, *12* (4), 196.

(41) Zhu, H.; Jiang, D.; Zhu, J.-J. High-resolution imaging of catalytic activity of a single graphene sheet using electrochemiluminescence microscopy. *Chem. Sci.* **2021**, *12* (13), 4794−4799.

(42) Khazalpour, S.; Nematollahi, D. Electrochemical study of Alamar Blue (resazurin) in aqueous solutions and room-temperature ionic liquid 1-butyl-3-methylimidazolium tetrafluoroborate at a glassy carbon electrode. *RSC Adv.* **2014**, *4* (17), 8431−8438.

(43) Yu, D.; Zha, Y.; Zhong, Z.; Ruan, Y.; Li, Z.; Sun, L.; Hou, S. Improved detection of reactive oxygen species by DCFH-DA: New insight into self-amplification of fluorescence signal by light irradiation. *Sens. Actuators, B* **2021**, *339*, No. 129878.

(44) Buglakova, E.; Ekelöf, M.; Schwaiger-Haber, M.; Schlicker, L.; Molenaar, M. R.; Shahraz, M.; Stuart, L.; Eisenbarth, A.; Hilsenstein, V.; Patti, G. J.; Schulze, A.; Snaebjornsson, M. T.; Alexandrov, T. Spatial single-cell isotope tracing reveals heterogeneity of de novo fatty acid synthesis in cancer. *Nat. Metab.* **2024**, *6* (9), 1695−1711.

(45) Luo, C.; Sun, J.; Liu, D.; Sun, B.; Miao, L.; Musetti, S.; Li, J.; Han, X.; Du, Y.; Li, L.; Huang, L.; He, Z. Self-Assembled Redox Dual-Responsive Prodrug-Nanosystem Formed by Single Thioether-Bridged Paclitaxel-Fatty Acid Conjugate for Cancer Chemotherapy. *Nano Lett.* **2016**, *16* (9), 5401−8.

(46) Allingham, J. S.; Smith, R.; Rayment, I. The structural basis of blebbistatin inhibition and specificity for myosin II. *Nat. Struct. Mol. Biol.* **2005**, *12* (4), 378−9.

(47) Képiró, M.; Várkuti, B. H.; Végner, L.; Vörös, G.; Hegyi, G.; Varga, M.; Málnási-Csizmadia, A. para-Nitroblebbistatin, the Non-Cytotoxic and Photostable Myosin II Inhibitor. *Angew. Chem., Int. Ed. Engl.* **2014**, *53* (31), 8211−8215.

(48) Li, M.-D.; Wong, N.-K.; Xiao, J.; Zhu, R.; Wu, L.; Dai, S.-Y.; Chen, F.; Huang, G.; Xu, L.; Bai, X.; Geraskina, M. R.; Winter, A. H.; Chen, X.; Liu, Y.; Fang, W.; Yang, D.; Phillips, D. L. Dynamics of Oxygen-Independent Photocleavage of Blebbistatin as a One-Photon Blue or Two-Photon Near-Infrared Light-Gated Hydroxyl Radical Photocage. *J. Am. Chem. Soc.* **2018**, *140* (46), 15957−15968.

(49) Zhang, Y.; Gong, X.; Yuan, Z.; Wang, W.; Chen, Y. C. DNA Self-Switchable Microlaser. *ACS Nano* **2020**, *14* (11), 16122−16130.